

Wide-bandwidth triboelectric energy harvester combining impact nonlinearity and multi-resonance method

Chaoyang Zhao ^a, Guobiao Hu ^b, Xin Li ^c, Zicheng Liu ^a, Weifeng Yuan ^{d,e}, Yaowen Yang ^{a,*}

^a School of Civil and Environmental Engineering, Nanyang Technological University, 50 Nanyang Avenue, 639798, Singapore

^b Thrust of Internet of Things, The Hong Kong University of Science and Technology (Guangzhou), Nansha, Guangzhou 511400, China

^c Advanced Manufacturing Technology Innovation Center, Xidian University, Guangzhou 510555, China

^d Key Laboratory of Testing Technology for Manufacturing Process, MOE, Shock and Vibration of Engineering Materials and Structures Key Laboratory of Sichuan

Province, Southwest University of Science and Technology, Mianyang 621010, China

^e School of Science, Xi'an University of Architecture and Technology, Xi'an 710055, China

HIGHLIGHTS

- Proposal of a novel wide-bandwidth triboelectric energy harvester.
- Investigation of impact nonlinearity and multi-resonance in harvester design.
- Experimental validation of electromechanical harvester model.
- Demonstration of powering ability of harvester in IoT networks.

ARTICLE INFO

Keywords:

Triboelectric
Wide bandwidth
Impact nonlinearity
Multi-resonance
Frequency locking

ABSTRACT

This paper presents a novel wide-bandwidth triboelectric energy harvester (WBTEH) that takes advantage of impact nonlinearity and multi-resonance. The harvester features a triboelectric transducer that operates in contact and separation mode, with two cantilever beams of different resonant frequencies connected to it. By exploiting the relative motion of the beams, the harvester achieves a broad bandwidth through the resonance shift caused by the impact and multi-resonance. A WBTEH prototype with a 3 mm gap between the triboelectric pair shows a total bandwidth of 4.3 Hz even at a low base excitation of 3 m/s^2 . The matched peaks and bandwidth in the frequency up-sweep and down-sweep tests demonstrate the excellent stability of the WBTEH. The frequency locking phenomenon with strong resonance occurs in the WBTEH when the displacement amplitude/gap ratio exceeds 1.48, which is beneficial for obtaining a continuous bandwidth and a high power output. An electromechanical model is formulated for parametric studies that investigate the effects of contact stiffness and damping on the performance of WBTEH. It is found that large impact stiffness and small damping can cause quasi-periodic motion, leading to a non-constant voltage output that should be prevented in the harvester design. The WBTEH is capable of powering wireless sensors, making it a potential candidate for Internet of Things (IoT) applications.

1. Introduction

In recent years, the energy harvesting technique has emerged as a viable solution to convert ambient energy sources into electricity, serving as distributed energy supply strategy in powering electronic sensors for structural health monitoring (SHM) and the internet of things (IoT). Vibration-based energy harvesting has attracted a lot of attention

since vibration sources are abundant in the surroundings. However, ambient vibration sources usually have broad bandwidth and exhibit randomness. Traditional vibration-based energy harvesters produce the largest power outputs at the resonance. A slight shift in the base excitation frequency could cause a tremendous drop in the power output. Therefore, wide bandwidth design for energy harvesters has become crucial. For piezoelectric energy harvesters (PEHs), many bandwidth-

* Corresponding author.

E-mail address: cwyang@ntu.edu.sg (Y. Yang).

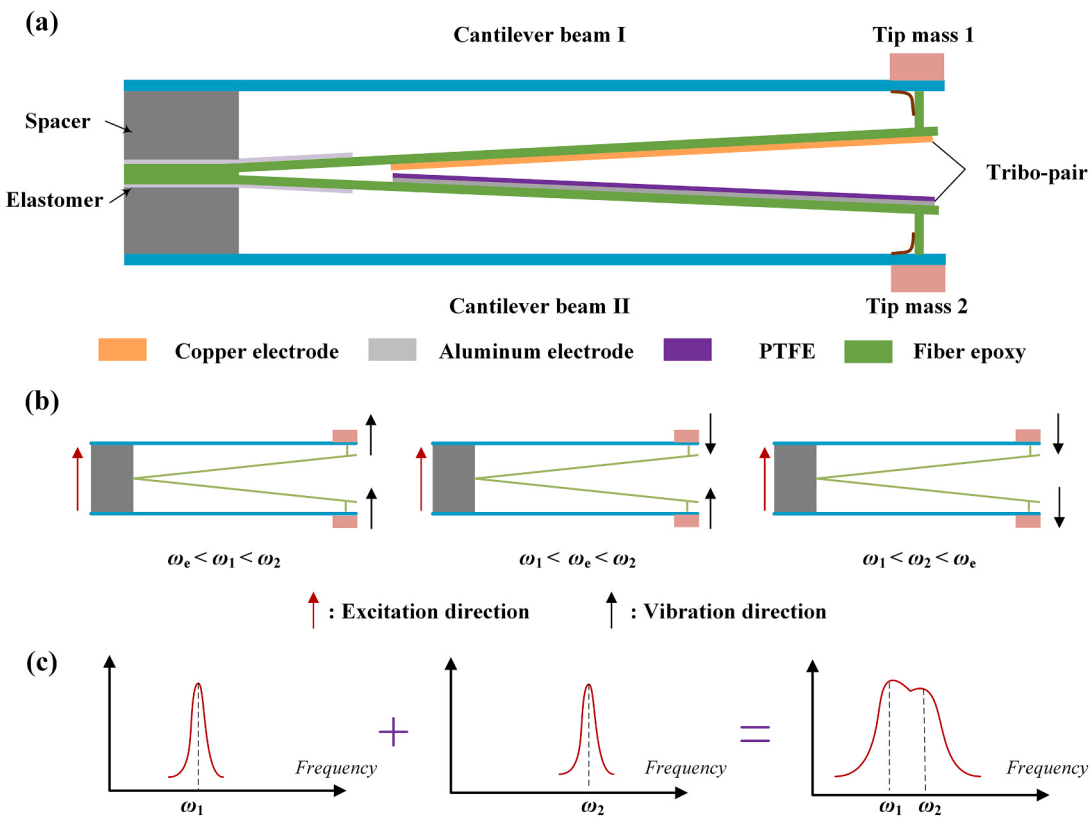


Fig. 1. a) The schematic diagram of the proposed WBTEH; b) illustration of the relative motions of different components at different excitation frequencies; c) the fundamental mechanism for bandwidth widening.

broadening techniques have been developed, such as resonance tuning techniques [1,2], multimodal methods [3,4], frequency up-conversion techniques [5], and nonlinear strategies [6,7]. On the contrary to using brittle piezoelectric material in PEH, triboelectric energy harvesters (TEHs) use flexible material as an alternative. TEHs have gained a lot of attraction due to their wide material selectivity, lightweight, and high power density even at low frequencies, making them a promising energy harvester for various application [8,9].

Most state-of-art TEH research focuses on materials innovation, for example, chemical and physical treatments to manipulate the surface morphonology of the triboelectric material to increase the effective contact area and boost the charge density [10,11]. From the perspective of structures, most works focused on designing the TEH for various energy sources such as wind [12,13], water flow [14,15], and raindrops [16,17]. However, there is limited research focused on the design of vibration TEHs concerning the bandwidth.

The energy generation mechanism of contact-separation mode TEHs relies on the contact and separation between two triboelectric layers. The layers experience impacts during structural vibrations, which cause stiffness hardening effect, resulting in resonance shifts and widened bandwidths. Some TEHs exploit impact nonlinearity to achieve wide bandwidths. For example, Dhakar et al. [18] proposed a TEH using a cantilever beam with the triboelectric energy generation component on its free end. They conducted both experimental and theoretical analyses and demonstrated that the TEH could generate 0.69 μW of power at 1 g acceleration with a 63% increase in bandwidth. Ibrahim et al. [19] investigated a TEH composed of upper aluminum and lower Polydimethylsiloxane (PDMS) layers. The aluminum sheet could oscillate under external excitation and trigger the contact and separation of the triboelectric layers. They concluded that the gap distance between the layers affects the bandwidth and voltage output of the TEH. Specifically, a larger gap results in a higher voltage output with a narrow bandwidth, while a smaller gap leads to a lower voltage output with a wider

bandwidth. Qi et al. [20] and Gupta et al. [21] introduced suspending blocks in their TEH design. The central blocks are supported by surrounding small beams, and the triboelectric pairs are constructed between the blocks and substrates with a gap. Notably, the purely impact-based TEHs always exhibit mismatched peaks and bandwidths during frequency up and down sweeping, indicating relatively poor stability.

Structural multistability is a promising method to achieve wide bandwidths with high stability. However, for contact-separation mode TEHs, the impact force induced could block the interwell oscillation with a large amplitude, making it difficult to achieve multistable oscillation. In contrast, Fu et al. [22] studied the dynamics and multistability of a sliding-mode TEH. Their harvester consisted of a cantilever beam, a slider, and magnets. A mathematical model was formulated with the consideration of the friction force. The results unveiled that a bistable system can achieve interwell oscillation at low frequencies, while a tristable system only produces intrawell oscillations, which is not beneficial for energy harvesting. Tan et al. [23] proposed a bow-type TEH for harnessing low-frequency vibration energy. Their harvester consists of two flexible beams and a base plate. Two rigid rods with hinges are used to connect the beams and the top slider on the base. Their prototype exhibited broad bandwidth characteristics owing to its bistability and produced an instantaneous power of 0.64 mW at 5 Hz. Luo et al. [24] reported a TEH that comprises a spring-link mechanism, guide rails, and slider blocks. The dipteran flight inspired the harvester design, and the spring-link mechanism imitated the flight state. The link lengths can adjust the potential barrier between the wells. Overall, most multistable TEHs were designed based on the sliding mode to avoid obstacles that could hinder interwell oscillation.

A contact-separation mode TEH has the potential to achieve maximum capacitance when its two triboelectric layers come into contact under external force, leading to higher energy conversion efficiency compared to a sliding mode TEH. While multistability has been utilized for sliding mode TEHs to widen the bandwidth, there is still a need to

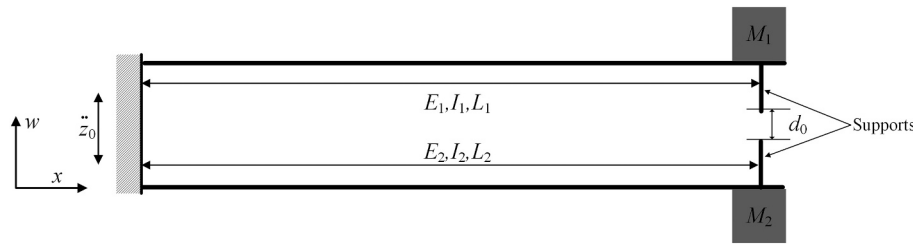


Fig. 2. The simplified model for the proposed WBTEH.

explore a wide-bandwidth contact-separation mode TEH that offers good stability. The multi-resonance method widens the bandwidth by generating multiple peaks [25,26]. Such a method can also be employed used for contact-separation mode TEHs to control the relative motion of triboelectric layers at various resonant frequencies. This study introduces a novel wide-bandwidth triboelectric energy harvester (WBTEH) that combines impact nonlinearity and multi-resonance method. An electromechanical model will be formulated for the developed WBTEH and its performance will be evaluated both experimentally and numerically. The structural design of WBTEH will be presented in [Section 2](#), followed by the theoretical model formulation in [Section 3](#). The experimental setup will be detailed in [Section 4](#), and the test results and discussion will be presented in [Section 5](#). The model validation will be demonstrated in the [Section 6](#), and the performance of the proposed WBTEH will be evaluated using a wireless sensing network in [Section 7](#). In the end, the major conclusions will be drawn.

2. Structural design overview

As shown in [Fig. 1\(a\)](#), the harvester comprises two cantilever beams with a spacer in between at the clamped end. Two middle plates are connected to the spacer using elastomer, which allows the plate to rotate around the left end. At the right end, the plate is connected to the cantilever beam by using support and flexible tape. Adjusting the spacer and support can control the gap distance at the right end. Two tip masses are attached on the free ends to tune the natural frequencies of the beams. The copper, aluminum, and PTFE film are used to construct the triboelectric pair between the two middle plates. The working mechanism of the energy generation component has already been discussed in our previous work [27]. In brief, the negative charge is generated on the surface of the PTFE film when it is in contact with the copper electrode. The vibration of the beam causes a regular contact and separation motion of the triboelectric pair. In this process, the charges flow back and forth between two electrodes, thus generating the alternating current (AC).

In [Fig. 1\(b\)](#), ω_1 and ω_2 represent the fundamental natural frequencies of cantilever beam I and II, respectively, and we intentionally designed them to satisfy $\omega_1 < \omega_2$. ω_e denotes the excitation frequency. The proposed WBTEH is designed based on the contact-separation mode of the triboelectric pair. The generated voltage highly depends on the relevant motion between the contact pair. Assume that the excitation sweeps from the low to high frequency. In the beginning, the vibration motions of the two beams are in-phase with the base excitation when $\omega_e < \omega_1 < \omega_2$. The vibration amplitude of beam I increases until it reaches the

ω_1 , i.e. $\omega_1 < \omega_e < \omega_2$, beam II still vibrates in phase with the excitation while beam I vibrates in anti-phase with excitation. At this stage, the two beams approach each other in the reverse direction until reaching the resonance of beam II, which makes easy contact between the triboelectric pair if the vibration amplitude and gap distance are properly configured. Once the excitation frequency exceeds ω_2 , both beams vibrate in anti-phase with the base excitation, and the vibration of beam II governs the energy harvesting performance in this range. A traditional TEH can only obtain high power output around its resonance with a single narrow peak. The proposed WBTEH has the potential to fully utilize the oscillations of two beam components and get two peaks ([Fig. 1\(c\)](#)). As a result, the harvester achieves a wide bandwidth. Meanwhile, adjusting the harvester parameters can tune the total bandwidth, which will be discussed in detail in the following sections.

3. Electromechanical modeling

3.1. Mechanical domain

Note that the middle plates are connected to the beams using flexible tapes rather than rigid hinges. The plates contribute to the additional mass added on the tip and have little influence on structure stiffness. Thus, the WBTEH can be simplified as a dual-beam system with supports, as shown in [Fig. 2](#). Considering that the beams are thin and have a large aspect ratio, the Euler-Bernoulli beam theory is employed to model the system [28,29], and the governing equations can be written as:

$$\left\{ \begin{array}{l} \frac{\partial^2}{\partial x^2} \left[E_1 I_1 \frac{\partial^2 w_1(xt)}{\partial x^2} \right] + c_{s1} I_1 \frac{\partial^5 w_1(xt)}{\partial x^4 \partial t} + c_{a1} \frac{\partial w_1(xt)}{\partial t} + m_1 \frac{\partial^2 w_1(xt)}{\partial t^2} \\ = -[m_1 + M_{t1} \delta(x-L)] \frac{d^2 z_0(t)}{dt^2} + F_c \delta(x-x_1) \\ \\ \frac{\partial^2}{\partial x^2} \left[E_2 I_2 \frac{\partial^2 w_2(xt)}{\partial x^2} \right] + c_{s2} I_2 \frac{\partial^5 w_2(xt)}{\partial x^4 \partial t} + c_{a2} \frac{\partial w_2(xt)}{\partial t} + m_2 \frac{\partial^2 w_2(xt)}{\partial t^2} \\ = -[m_2 + M_{t2} \delta(x-L)] \frac{d^2 z_0(t)}{dt^2} - F_c \delta(x-x_1) \end{array} \right. \quad (1)$$

where E_1 , E_2 , and I_1 , I_2 are the Young's moduli and moments of inertia of the two beams, respectively. The subscripts 1 and 2 denote the cantilever beam I and II, respectively. C_{s1} , C_{s2} , and C_{a1} , C_{a2} refer to viscous and air damping coefficients, respectively. m_1 and m_2 denote the mass per unit length of beams. M_{t1} and M_{t2} are the tip masses, and F_c denotes the impact force that can be represented as [30,31]:

$$F_c = \begin{cases} 0, & w_2(x_1, t) - w_1(x_1, t) - d_0 \leq 0 \\ k_c(w_2(x_1, t) - w_1(x_1, t) - d_0) + c_c(v_2(x_1, t) - v_1(x_1, t)), & w_2(x_1, t) - w_1(x_1, t) - d_0 > 0 \end{cases} \quad (2)$$

maximum at its resonance, and the vibration of beam I dominates the generated voltage at this stage. When the excitation frequency exceeds

where k_c and c_c are the impact stiffness and damping coefficient, respectively. d_0 denotes the initial gap distance. x_1 is the impact location

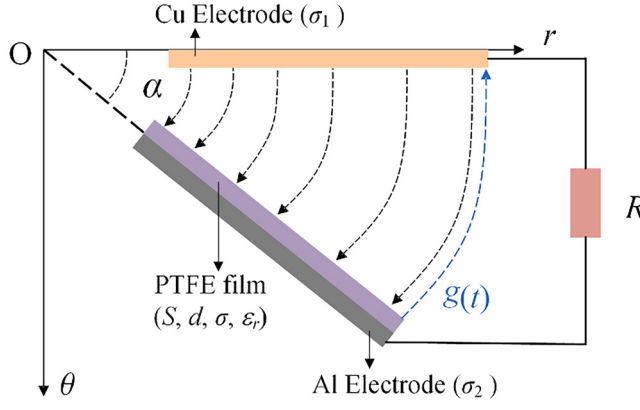


Fig. 3. The electrical model for the proposed WBTEH.

on the beam. Eq. (2) assumes that there is no impact force when the relative motion of beams is smaller than the initial gap distance. The force will only be included once the relative displacement exceeds the gap distance. Furthermore, the governing equation does not include the contribution of the electrostatic force due to the relatively small surface charge density observed. Fu et al. [32] has reported that significant backward coupling, specifically from the electrical domain to the mechanical domain, becomes noticeable only when the surface charge density exceeds $50 \mu\text{C}/\text{m}^2$. In the present study, the surface charge density of the triboelectric material used is smaller than $3 \mu\text{C}/\text{m}^2$, indicating a relatively weak backward coupling effect. Eq. (1) is a set of partial differential equations (PDEs) that can be solved using the variable-separation approach. Assume that the deflection solution has the form:

$$w_i(x, t) = \phi_{i,r}(x)\eta_{i,r}(t) \quad (3)$$

where $\phi_{i,r}(x)$ and $\eta_{i,r}(t)$ are the r^{th} modal shape and modal coordinate of the beams, in which, $i = 1, 2$ represents beam I and beam II. To obtain the natural frequencies and modal shapes of the beam, Eq. (1) is simplified by ignoring the damping force terms as

$$E_i I_i \frac{\partial^4 w_i(x, t)}{\partial x^4} + m_i \frac{\partial^2 w_i(x, t)}{\partial t^2} = 0 \quad (4)$$

Note that the harvester is clamped, and the other end with a tip mass is freely hanging. The boundary conditions for the clamped-free beam components are

$$\begin{cases} w_i(0, t) = 0 \\ \left. \frac{\partial w_i(x, t)}{\partial x} \right|_{x=0} = 0 \\ E_i I_i \left. \frac{\partial^2 w_i(x, t)}{\partial x^2} \right|_{x=L} = 0 \\ E_i I_i \left. \frac{\partial^3 w_i(x, t)}{\partial x^3} \right|_{x=L} = 0 \end{cases} \quad (5)$$

Substituting Eq. (3) into Eq. (4) and considering the boundary conditions in Eq. (5), the eigen-function of the r^{th} mode for beam i can be obtained as

$$\phi_{i,r} = C_{i,r} \left[\cosh \frac{\lambda_{i,r}}{L} x - \cos \frac{\lambda_{i,r}}{L} x - \sigma_{i,r} \left(\sin \frac{\lambda_{i,r}}{L} x - \sinh \frac{\lambda_{i,r}}{L} x \right) \right] \quad (6)$$

where

$$\sigma_{i,r} = \frac{m_i L (\sin \lambda_{i,r} - \sinh \lambda_{i,r}) + \lambda_{i,r} M_{t,i} (\cos \lambda_{i,r} - \cosh \lambda_{i,r})}{m_i L (\cos \lambda_{i,r} + \cosh \lambda_{i,r}) - \lambda_{i,r} M_{t,i} (\sin \lambda_{i,r} - \sinh \lambda_{i,r})} \quad (7)$$

The eigenvalues are the roots of the following characteristic

equation, in which the rotary inertia of the tip mass ($I_{t,i}$) is considered.

$$1 + \cos \lambda_{i,r} \cosh \lambda_{i,r} + \frac{\lambda_{i,r} M_{t,i}}{m_i L} (\cos \lambda_{i,r} \sinh \lambda_{i,r} - \sin \lambda_{i,r} \cosh \lambda_{i,r}) - \frac{\lambda_{i,r}^3 I_{t,i}}{m_i L^3} (\cosh \lambda_{i,r} \sin \lambda_{i,r} + \sinh \lambda_{i,r} \cos \lambda_{i,r}) + \frac{\lambda_{i,r}^4 M_{t,i} I_{t,i}}{m_i 2 L^4} (1 - \cos \lambda_{i,r} \cosh \lambda_{i,r}) = 0 \quad (8)$$

The modal coefficient $C_{i,r}$ of the r^{th} mode can be obtained by using below orthogonality conditions:

$$\begin{aligned} & \int_0^L \phi_{i,s}(x) m_i \phi_{i,r}(x) dx + \phi_{i,s}(L) M_{t,i} \phi_{i,r}(L) + \left[\frac{d\phi_{i,s}(x)}{dx} I_{t,i} \frac{d\phi_{i,r}(x)}{dx} \right]_{x=L} \\ &= \delta_{i,rs} \int_0^L \phi_{i,s}(x) E_i I_i \frac{d^4 \phi_r(x)}{dx^4} dx - \left[\phi_{i,s}(x) E_i I_i \frac{d^3 \phi_{i,r}(x)}{dx^3} \right]_{x=L} \\ &+ \left[\frac{d\phi_{i,s}(x)}{dx} E_i I_i \frac{d^2 \phi_{i,r}(x)}{dx^2} \right]_{x=L} \\ &= \omega_{i,rr}^2 \delta_{i,rs} \end{aligned} \quad (9)$$

where $\delta_{i,rs}$ is the Dirac function that has the values:

$$\delta_{i,rs} \begin{cases} 0, & r \neq s \\ 1, & r = s \end{cases} \quad (10)$$

and $\omega_{i,rr}$ is the modal frequency that can be represented by:

$$\omega_{i,rr} = \lambda_{i,r} \sqrt{\frac{E_i I_i}{m_i L^4}} \quad (11)$$

Subsequently, the governing equation of the system can be reformulated in the modal coordinate form as:

$$\begin{aligned} & \frac{d^2 \eta_{1,r}(t)}{dt^2} + 2\zeta_{1,r} \omega_{1,r} \frac{d\eta_{1,r}(t)}{dt} + \omega_{1,r}^2 \eta_{1,r}(t) = f_{base,1} + f_c \\ & \frac{d^2 \eta_{2,r}(t)}{dt^2} + 2\zeta_{2,r} \omega_{2,r} \frac{d\eta_{2,r}(t)}{dt} + \omega_{2,r}^2 \eta_{2,r}(t) = f_{base,2} - f_c \end{aligned} \quad (12)$$

in which

$$f_{base,i} = - \left[\int_0^L \phi_{i,r}(x) m_i dx + \phi_{i,r}(L) M_{t,i} \right] \frac{d^2 z_0(t)}{dt^2} \quad (13)$$

and

$$f_c = \begin{cases} 0 \\ w_2(x_1, t) - w_1(x_1, t) - d_0 \leq 0 \\ \phi_{i,r}(x) [k_c(w_2(x_1, t) - w_1(x_1, t) - d_0) + c_c(v_2(x_1, t) - v_1(x_1, t))] \\ , w_2(x_1, t) - w_1(x_1, t) - d_0 > 0 \end{cases} \quad (14)$$

3.2. Electrical domain

The electrical model should consider the non-parallel triboelectric layers with an angle (α) as shown in Fig. 3. According to our previous work [27], the model can be established based on the V - Q - x relations of the harvester, which is:

$$R \frac{dQ}{dt} + \frac{Q}{Se_0} \left(\frac{d}{\epsilon_r} + \mu g(t) \right) - \frac{\sigma \mu g(t)}{\epsilon_0} = 0, Q(t=0) = 0 \quad (15)$$

where, R is the resistance of the external load. Q denotes the transferred charge between two electrodes. S and d are the surface area and the thickness of the triboelectric material, respectively. ϵ_0 and ϵ_r are the vacuum permittivity and relative permittivity of the triboelectric material. σ is the surface charge density of the material. $\sigma = \sigma_1 + \sigma_2$, in which σ_1 and σ_2 represent the charge density of the Cu and Al electrodes, respectively. μ represents the equivalent coefficient related to the

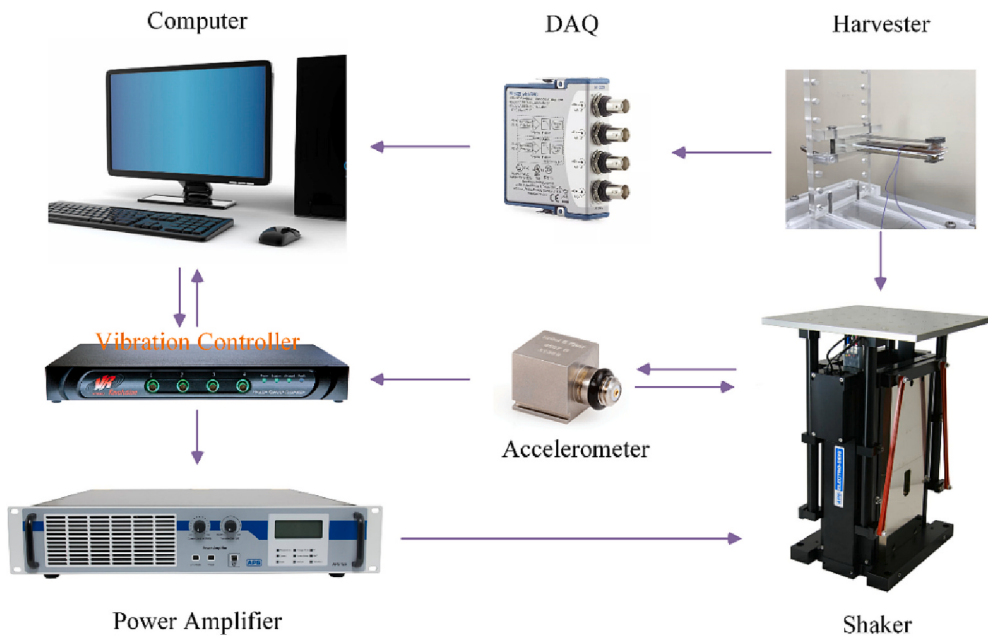


Fig. 4. Diagram of the experimental setup.

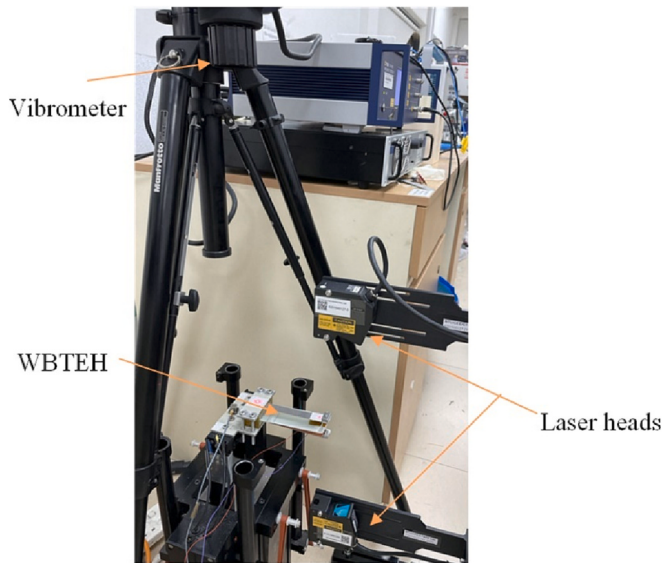


Fig. 5. The equipment setup, including two laser heads and a vibrometer, for measuring the WBTEH prototype's dynamic response.

triboelectric pair's geometrical dimension. $g(t) = w_2(x_1, t) - w_1(x_1, t) - d_0$, then, the mechanical model and electrical model are coupled by the term $g(t)$.

4. Experimental setup

The WBTEH prototype was fabricated and tested in the experiment to examine its electricity generation performance. The cantilever beam is made of aluminum owing to its excellent machinability. Lightweight fiber epoxy sheets are used to fabricate the middle plate, and the acrylic sheet works as the spacer. The test setup is shown in Fig. 4. The harvester is mounted on the shaker that simulates the ambient base excitation. The controller generates a harmonic excitation, and the output vibration signal is then amplified by a power amplifier, which finally drives the shaker to vibrate. An accelerometer is attached to the shaker to monitor

the vibration acceleration and feedback to the controller. The magnitude of the base excitation ranges from 3 m/s^2 to 6 m/s^2 in the test. The excitation frequency sweeps from 14 Hz to 26 Hz with a sweeping speed of 0.1 Hz/s. A data acquisition (DAQ) system acquires the voltage output of the WBTEH prototype.

In order to have a better understanding of the dynamic behavior of the WBTEH when impact happens and to facilitate the parameter determination in the model validation, laser sensors are utilized to measure the vibration displacement of the beams. Fig. 5 shows the overall experiment setup. Two Keyence LK-H157 laser heads are mounted on an adjustable stand, ensuring a good alignment between the sensors and beams. The WBTEH prototype is placed between those sensors. The data acquisition frequency is configured to be 5 kHz to capture the dynamic behavior of the beams before and after the impact. Besides, a Doppler vibrometer (Polytec FOV-503) measures the vibration of the shaker. The absolute vibration displacement of the two beams could be obtained by post-processing the data from the laser heads and the vibrometer.

5. Results and discussion

5.1. WBTEH with various gaps

The energy generation of TEH is based on the contact and separation of triboelectric layers, and the initial gap distance between the layers affects the contact status of the triboelectric pair and thus the electricity output. Therefore, the WBTEHs with various initial gap distances are tested using the established experimental platform. For ease of narration, a notion is adopted in this section to represent the WBTEH in different configurations. WBTEH-X-Y-Z, in which X ($= 5 \text{ mm}, 3 \text{ mm}, 2 \text{ mm}, \text{ and } 0 \text{ mm}$) denotes the gap distances, Y ($= 3 \text{ m/s}^2, 4 \text{ m/s}^2, 5 \text{ m/s}^2, \text{ and } 6 \text{ m/s}^2$) stands for the magnitude of base acceleration, and Z is the excitation frequency. Fig. 6 shows the root mean square (RMS) voltage (V_{rms}) of different WBTEH models at different testing conditions. For WBTEH-5 mm (Fig. 6(a)), two voltage peaks are observed at different base accelerations. Note that most of the test cases achieve the best energy output at the resonance with the largest amplitudes that can enhance the contact of triboelectric pair and convert more kinetic energy into electricity. The left peak occurs at the resonant frequency of beam I ($\omega_{n1} = 18.4 \text{ Hz}$), and the right peak corresponds to the resonant

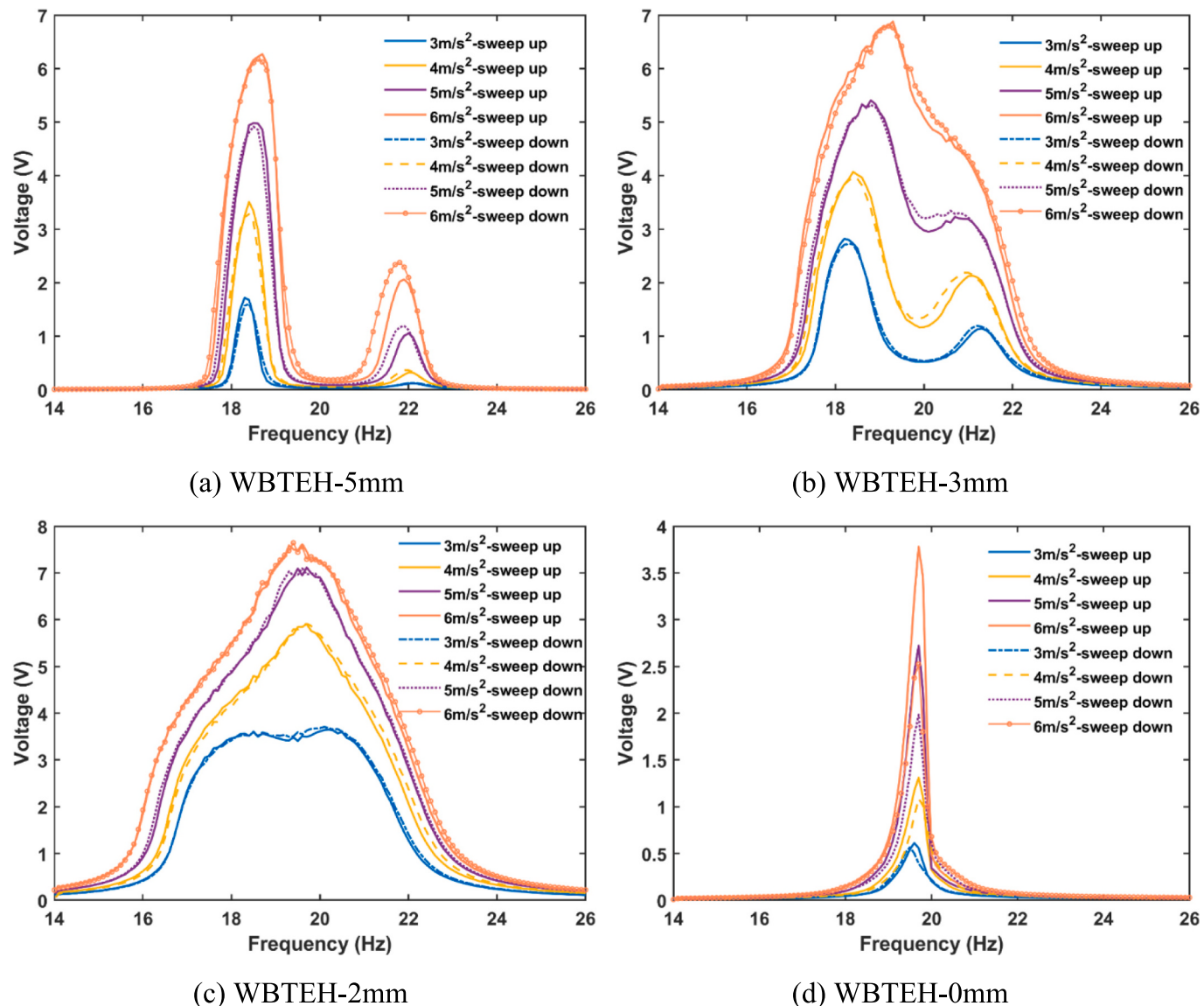


Fig. 6. Experimental results of different WBTEH prototypes under various base excitations: (a) gap = 5 mm; (b) gap = 3.5 mm; (c) gap = 2 mm; (d) gap = 0 mm.

frequency of beam II ($\omega_{n2} = 22.1$ Hz). Compared to the traditional one-degree-of-freedom (1DOF) harvester with only a single voltage peak, the proposed WBTEH has dual resonance. Thus, the bandwidth is broadened in a sense. However, there is a frequency range that the voltage output is relatively small between those two peaks. If taking $V_{rms} = 0.2$ V as a threshold, the WBTEH-5 mm- 3 m/s^2 produces $V_{rms} < 0.2$ V from 19 Hz to 21.5 Hz. This range can be narrowed by increasing the base excitation. For example, the corresponding range is shortened from 19.8 Hz to 20.8 Hz for WBTEH-5 mm- 6 m/s^2 . A clear trend is that V_{rms} increases with the base excitation. Assume that the surface charge density is constant, the generated voltage should depend on the charge transfer speed. A large acceleration produces intense vibration and makes the triboelectric layers in contact with high speed, leading to the generation of more electricity. It can also be observed that the magnitude of the second peak is lower than the first peak because beam II has a smaller vibration amplitude at a relatively high frequency, corresponding to a lower impact speed. When reducing the gap distance, such as WBTEH-3 mm, V_{rms} increment for the second peak is obvious compared to WBTEH-5 mm. For instance, WBTEH-3 mm- 5 m/s^2 shows a tremendous growth of $V_{rms} = 3$ V at $\omega_e = 20$ Hz. Fig. 6(b) shows a clear trend that two peaks get closer with increased base excitation. The reason is that the impact could

change the beam stiffness, resulting in the resonant frequency shift, especially under large base excitation. WBTEH-3 mm- 3 m/s^2 exhibits two shifted peaks, i.e., $\omega_{n1} = 18.3$ Hz and $\omega_{n2} = 21.3$ Hz. The frequency shift becomes more obvious for WBTEH-2 mm- 3 m/s^2 with a smaller gap (Fig. 6(c)).

Fig. 6(d) shows the results of the model with the triboelectric layers initially in contact, i.e., the gap distance is approximately equal to zero. It could be observed that significant V_{rms} is only produced over a narrow frequency range, which is quite different from the models with non-zero gaps. Initial contact results in the overall increase of the stiffness even though they are not perfectly bonded together. When the base excitation frequency gradually reaches the resonance, the separation and contact of the two beams occur, thus giving a very sharp voltage output. Once the excitation frequency moves out of the resonance, the vibration of the harvester attenuates dramatically, and effective separation of the triboelectric pair is difficult to be guaranteed, leading to a feeble voltage output. The downward frequency sweeping test is also carried out to examine the stability. Unlike the traditional wide-bandwidth TEH with mismatched peaks, the results for both frequency up-sweep and down-sweep cases almost overlap for WBTEH with a non-zero gap, demonstrating its excellent stability. There is an exception for WBTEH-0 mm. In

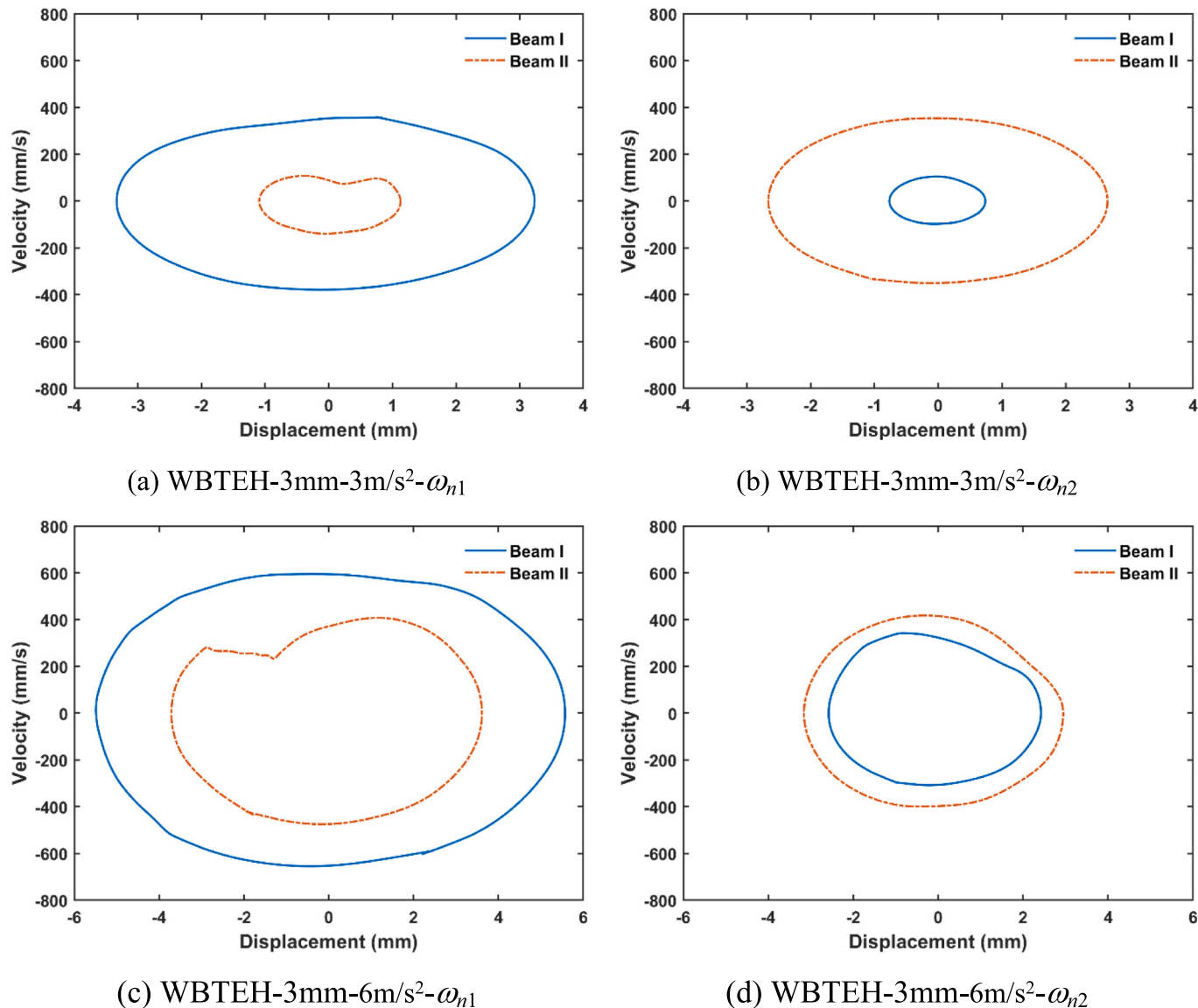


Fig. 7. Phase diagram of the WBTEH-3 mm working under different conditions: (a) resonance of beam I under 3 m/s^2 ; (b) resonance of beam II under 3 m/s^2 ; (c) resonance of beam I under 6 m/s^2 ; (d) resonance of beam II under 6 m/s^2 .

such a case, the harvester generates a noticeably lower V_{rms} during the down-sweep process, although the frequencies for the maximum V_{rms} are similar. The reason is attributed to the strong nonlinearity of the system, and the beam components come into impact with lower energy during frequency down-sweep.

Fig. 7(a) and (b) present the phase diagrams of the WBTEH-3 mm working at the two resonances. In Fig. 7(a), the amplitude of beam I is larger than the gap distance (3 mm). A remarkable change occurs in the phase trajectory of beam II caused by the impact with beam I. In this scenario, beam I has relatively large vibration velocity and displacement compared to beam II. Consequently, beam I is less influenced by the impact, as indicated by the phase trajectories. The change can not be observed for WBTEH-3 mm-3 m/s²- ω_{n2} in Fig. 7(b) since there is no impact. The different voltage output behaviors at the two resonances verify the positive effect of impact for generating a higher voltage because the impact improves the contact of triboelectric layers and benefits the charge transformation. The amplitude growth of both beams is attributed to the large base excitation. As a result, the impact can also occur at the resonance of beam II (Fig. 7(d)). Meanwhile, the trajectory change of beam II becomes even more obvious at the resonance of beam

I (Fig. 7(c)).

Besides, it is found that the two peaks merge together when the base acceleration goes up to 6 m/s^2 , and there is only one clear peak ($\omega = 19.2 \text{ Hz}$), and the second peak becomes unnoticeable (Fig. 6(b)). The frequency merge can also be observed for WBTEH-2 mm with a narrower gap and under even a lower base excitation, such as WBTEH-2 mm-4 m/s² in Fig. 6(c). Further increasing the base acceleration beyond 4 m/s^2 does not cause any peak frequency shift. Such a phenomenon is similar to a type of nonlinear resonance called "frequency locking", for which the impact energy is transferred to the whole system, and strong resonance will occur [33]. At the locking frequency, the vibration amplitudes of the two beams are similar (Fig. 8(a)). Fig. 8(b) shows that the phase trajectories of the beams almost overlap except for the part where the impact happens. At this frequency, there is a strong coupling between the two beams, resulting in noticeable changes in the phase trajectories for both beams. The highly asymmetric voltage output profile in Fig. 8(a) also proves the nonlinearity of the system when strong resonance occurs. The maximum V_{rms} of 7.6 V is obtained at the locking frequency for WBTEH-2 mm-6 m/s².

As discussed, the frequency locking phenomenon always occurs

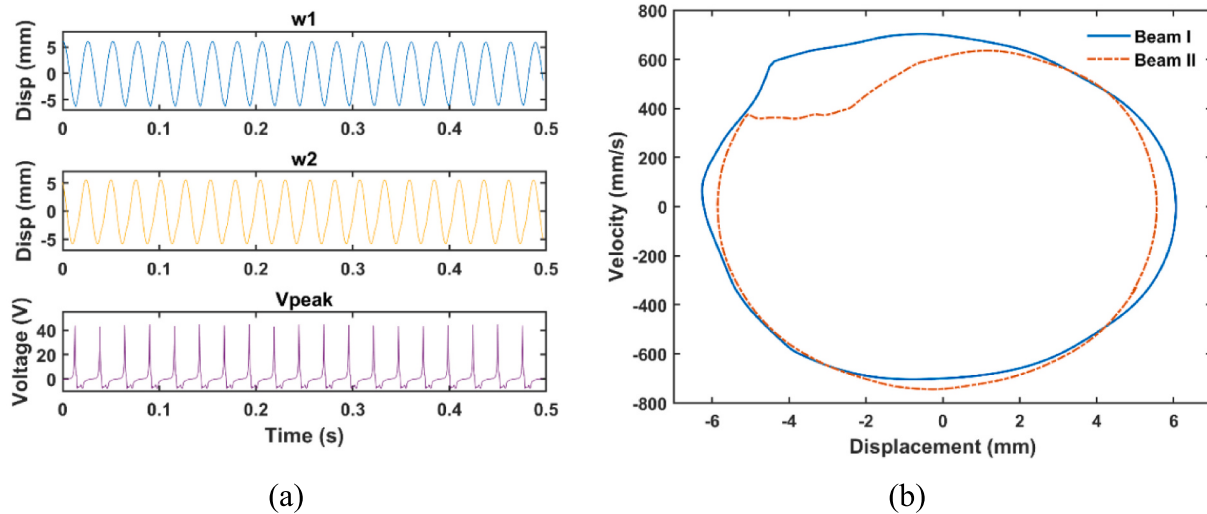


Fig. 8. (a) Displacement of two beams and peak voltage output for WBTEH-2 mm-6 m/s² at locking frequency; (b) corresponding phase diagram of two beams.

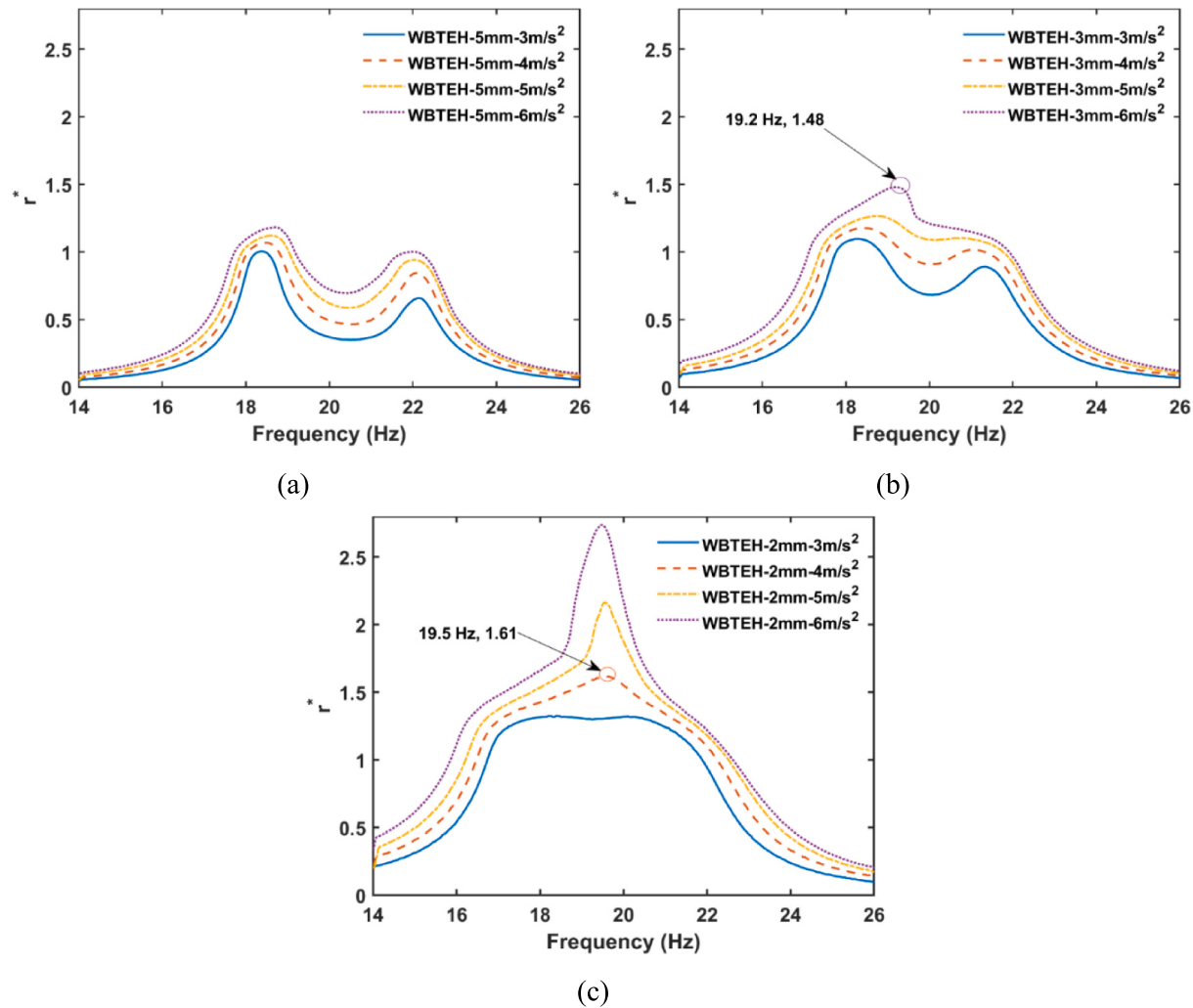


Fig. 9. r^* as a function of the frequency for WBTEH-5 mm, WBTEH-3 mm, and WBTEH-2 mm.

along with large-amplitude strong resonance. The proposed WBTEH energy generation is based on the relative motion between two triboelectric layers. A dimensionless parameter r^* is defined to understand the condition to trigger the frequency locking. $r^* = A_{21}/d_0$, in which A_{21}

is the amplitude of the relative motion between two beams measured in the experiment and d_0 is the initial gap distance. Fig. 9 shows the r^* values for the tested WBTEHs except for WBTEH-0 mm, which has a quasi-zero initial gap distance with an infinite r^* value. As shown in

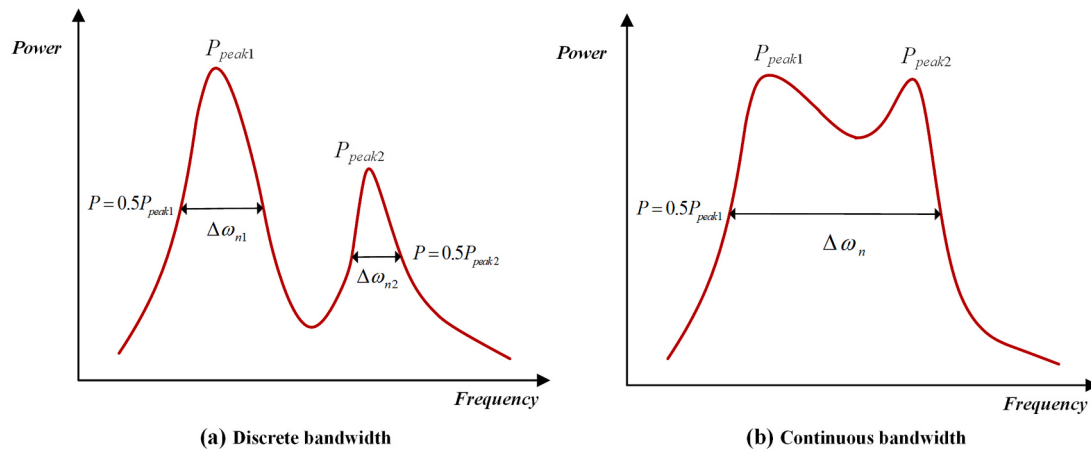


Fig. 10. Bandwidth definition: (a) Discrete bandwidth; (b) Continuous bandwidth.

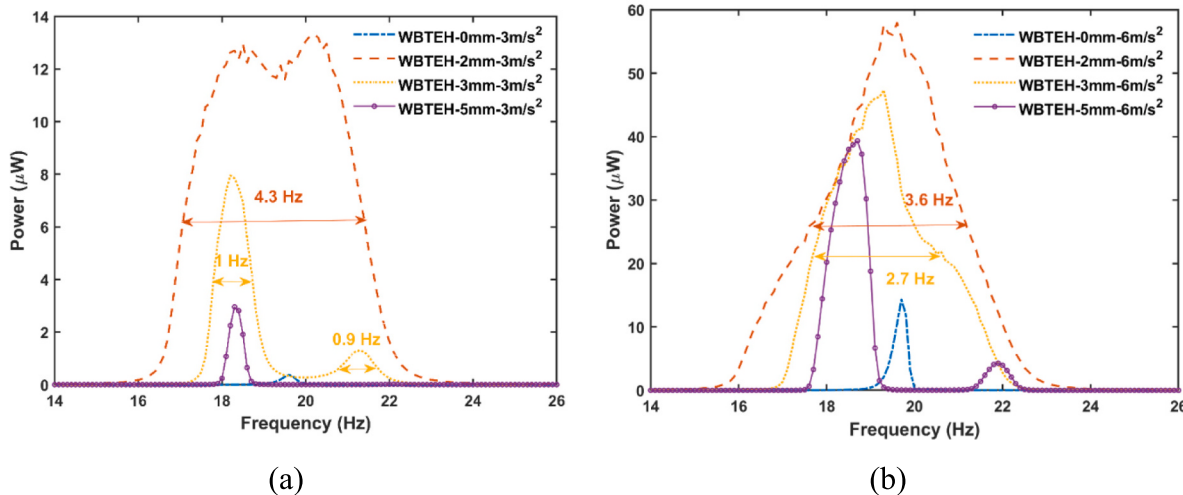


Fig. 11. Bandwidth analysis for WBTEHs with various gaps working under the base excitation of (a) 3 m/s²; (b) 6 m/s².

Fig. 9(b) and (c), frequency locking occurs for WBTEH-3 mm-6 m/s² at $r^* = 1.48$ and WBTEH-2 mm-4 m/s² at $r^* = 1.61$, although their locking frequencies are slightly different. One can conclude that $r^* \approx 1.48$ is the threshold for triggering such a phenomenon. For $r^* < 1.48$, e.g., the WBTEH-5 mm, two peaks are clearly separated without frequency locking. Essentially, r^* can estimate the level of impact nonlinearity and the extent of coupling between the beams. It provides valuable insights into the impact dynamics and the coupling effect within the harvester system.

5.2. Bandwidth analysis

Half-power bandwidth is widely used in energy harvesting to determine the harvesting bandwidth. As shown in Fig. 10, it is difficult to define the total bandwidth using a single peak if multiple peaks have various magnitudes. Hence, the bandwidth for each peak should be counted individually, which is called discrete bandwidth. The total bandwidth is the summation of discrete bandwidths. For example, the overall bandwidth should be $\Delta\omega_{n1} + \Delta\omega_{n2}$ in Fig. 10(a). If P_{peak2} climbs to a similar magnitude with P_{peak1} , a continuous bandwidth $\Delta\omega$ is obtained (Fig. 10(b)). In such a case, not only a broadened bandwidth is achieved, i.e., $\Delta\omega > (\Delta\omega_{n1} + \Delta\omega_{n2})$, but also a higher power is obtained at the second peak.

Note that the load resistance is 1 M\$\Omega\$, and the output power can be evaluated by $P = V_{rms}^2/R$. Fig. 11 shows the bandwidths of the WBTEHs.

Discrete bandwidth can be obtained for WBTEHs with large gaps at low base acceleration. For example, WBTEH-3 mm-3 m/s² has a total bandwidth of 1.9 Hz. The discrete bandwidth changes to continuous bandwidth when the base excitation reaches 6 m/s² and the total bandwidth goes up to 2.7 Hz, indicating that the base excitation affects not only the power output but also the bandwidth. The bandwidth of the WBTEH is also sensitive to the gap distance. A continuous bandwidth can be obtained by reducing the gap. For example, WBTEH-2 mm-3 m/s² has a continuous bandwidth of 4.3 Hz. The wide bandwidth achieved at low excitation levels in the proposed WBTEH demonstrates its superiority over traditional TENG devices in terms of both bandwidth and stability. For instance, Dhakar et al. [18] reported a broadband TEH with a bandwidth of approximately 5 Hz, while Ibrahim et al. [19] investigated a TEH with a bandwidth exceeding 8 Hz. Although their absolute bandwidth values are larger than those achieved in this work, it is important to note that their harvesters attain such bandwidth under excitations exceeding 6 m/s² and experience mismatched peaks during frequency up-sweeps and down-sweeps. In contrast, the proposed WBTEH exhibits wide-bandwidth characteristics under an excitation level of only 3 m/s², which is commonly encountered in ambient environments. Moreover, the WBTEH demonstrates good stability during frequency up-sweeps and down-sweeps, which is a rare achievement for traditional nonlinear impact-based TEH devices. This stability enhances the reliability and effectiveness of our WBTEH compared to existing literature in the field of wide-bandwidth TENG. The frequency locking

Table 1
Three groups of tip mass configuration.

	Group-A	Group-B	Group-C
M_{t1}	5.4 g	5.0 g	5.0 g
M_{t2}	3.0 g	3.0 g	3.2 g

phenomenon happens in WBTEH-2 mm-6 m/s² and induces the highest power output. However, the continuous bandwidth narrows to 3.6 Hz as the excitation increases from 3 to 6 m/s². It can be seen that there is a trade-off between power output and wide bandwidth. For the proposed WBTEH, 2 mm could be an optimal gap distance, which results in a relatively continuous wide bandwidth and generates significantly high power.

5.3. Effect by tuning mass

Based on the analysis from the last section, it can be concluded that the power output of the WBTEH depends on the contact-separation status of the triboelectric pair. Under the same excitation, one can tune the gap distance to control the contact status. Another approach is to tune the natural frequency of the beam to control the vibration amplitude at a given excitation. Natural frequencies can be adjusted by manipulating either the stiffness or mass. The beam stiffness effect is not discussed in this work, as precisely tuning the beam stiffness is difficult to realize in practice. The variation of beam stiffness eventually leads to the change of the natural frequency and amplitude, which has a similar effect to tuning the mass. Therefore, mass tuning is carried out in the test. Three groups of mass pairs are selected for WBTEH-3 mm and tested under different base excitations. Table 1 summarizes the detailed mass configurations in the test.

A notation WBTEH-X-Y followed by the mass group label is used in Fig. 12. For WBTEH-X-Y-A, two clear peaks can be observed in the voltage plot, and a discrete bandwidth is obtained. WBTEH-X-Y-B has a reduced mass M_{t1} as compared to WBTEH-X-Y-A. As a result, the two peaks get closer. When the base excitation goes up to 5 m/s², frequency locking occurs, and a continuous bandwidth is obtained for WBTEH-3 mm-5 m/s²-B. The bandwidth is also slightly wider than that of WBTEH-3 mm-5 m/s²-A. By increasing the mass M_{t2} in group C, the two peaks get even closer, and frequency locking shows up at a lower acceleration of 4

m/s². WBTEH-3 mm-5 m/s²-C has the same continuous bandwidth as WBTEH-3 mm-5 m/s²-B. However, adopting mass group C yields larger peak voltage and power. It can be concluded that the WBTEH performance is also sensitive to the tip masses because they change the resonant frequencies of the beams and the oscillation amplitudes, which thus affect the contact-separation status between the triboelectric pair. Continuous bandwidths can be obtained by carefully tuning the tip masses without adjusting the gap distance between the two beams.

6. Model validation

The formulated electromechanical model is solved numerically in MATLAB. The computed first three resonant frequencies are listed in Table 2. Note that for both beams, their 2nd resonant frequencies are

Table 2
Computed resonant frequencies of the two beams.

	1st mode (Hz)	2nd mode (Hz)	3rd mode (Hz)
Beam I	18.38	315.88	1407.40
Beam II	22.15	405.22	1439.50

Table 3
Mechanical and electrical parameters used in the modeling.

Parameters	Values
Beam dimensions (I&II)	100 × 15 × 0.8 mm ³
Mass density of beams I&II	2700 kg/m ³
Young's modulus of beams I&II	69 GPa
Air density	1.1644 kg/m ³
Location of motion transmission support, x_1	95 mm
Laser measurement location, x_m	90 mm
Tip mass 1, M_{t1}	5.4 g
Tip mass 2, M_{t2}	3.0 g
PTFE film dimensions	80 × 30 × 0.1 mm ³
Copper film dimensions	80 × 30 × 0.25 mm ³
Al foil dimensions	80 × 30 × 0.1 mm ³
Vacuum permittivity, ϵ_0	8.854×10^{-12} F/m
Relative permittivity of PTFE, ϵ_r	2.1
Thickness of PTFE, d	0.1 mm
External resistance, R	1 MΩ
Equivalent coefficient, μ	0.013

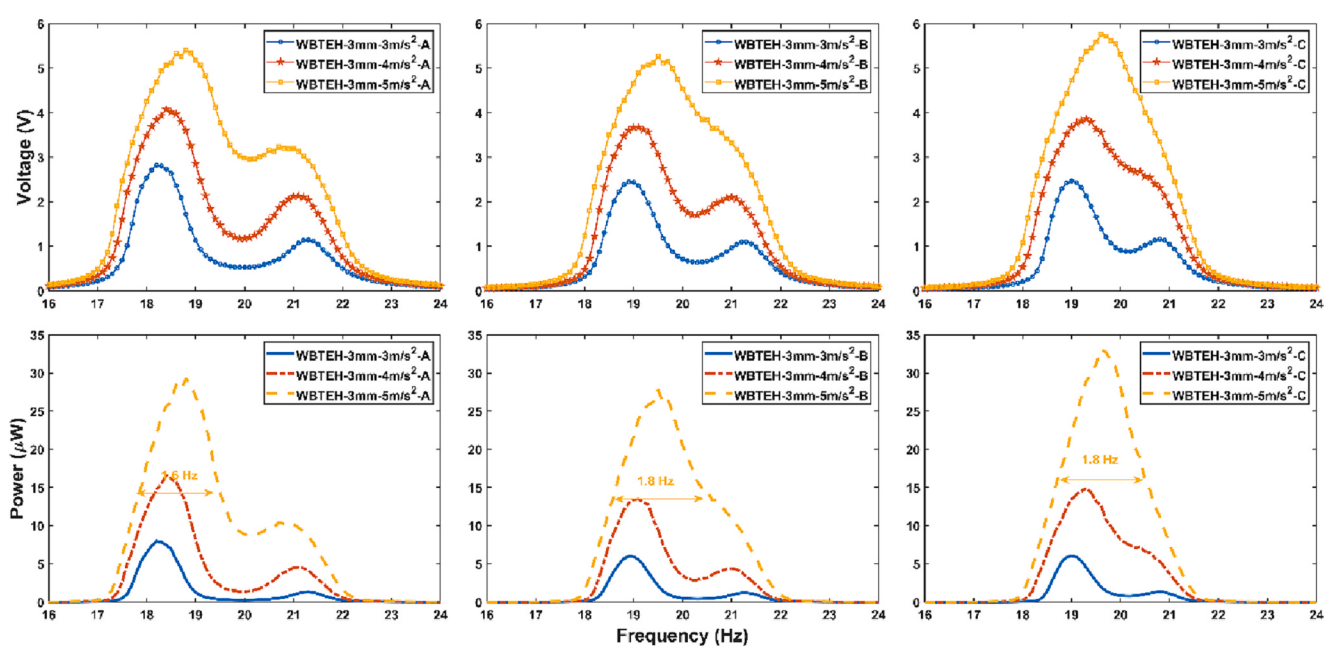


Fig. 12. Voltage and power outputs of the WBTEHs with differently configured tip masses under various base excitations.

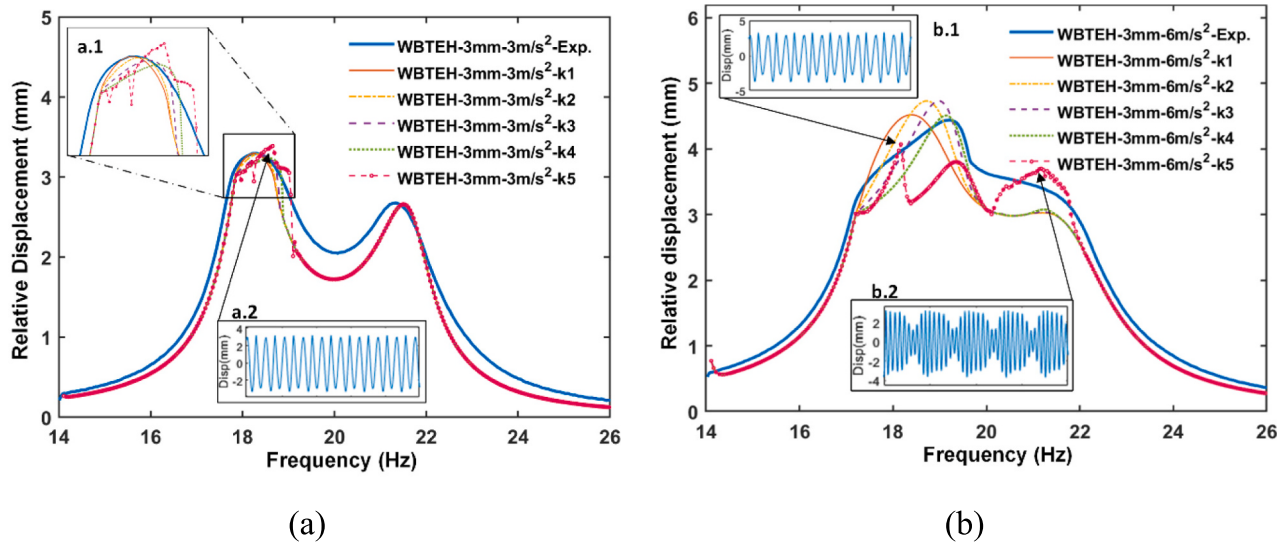


Fig. 13. Influence of impact stiffness on the dynamic response of the WBTEH.

much higher than their 1st resonant frequencies. Since the proposed WBTEH targets harnessing energy from a low-frequency source, the simulation only involves their 1st modes. *Al* sheets with known density and Young's modulus are utilized to fabricate the beams. The middle plates are connected to the beams using flexible materials, and only their weights are considered and added to the tip mass. The damping ratio is determined using the logarithmic attenuation method and tuned within a reasonable margin [34]. The surface charge density of PTFE is determined by measuring the effectively transferred charges using an electrometer (Keithley 6517B). In the absence of impact, the beam vibration is measured using a laser system, and the natural frequencies are determined experimentally. The model parameters are slightly adjusted to match the experimentally obtained natural frequencies and vibration amplitudes. The mechanical and electrical parameters of WBTEH are listed in Table 3. The WBTEH-3 mm series includes all the typical features, i.e., an example with the discrete bandwidth (WBTEH-3 mm-3 m/s²), and an example with the continuous bandwidth and frequency locking (WBTEH-3 mm-6 m/s²). Therefore, WBTEH-3 mm series models are taken as examples to validate the formulated model. The impact stiffness and damping coefficient are critical factors in evaluating the impact dynamics, thus relevant parametric studies are conducted.

6.1. Impact stiffness and damping

In this work, the impact force is introduced in the model using the force integration method (FIM), considering that the impact happens between two flexible components. For the FIM, the impact force is proportional to the impact stiffness and damping coefficient, which need to be properly selected in the model validation. Fig. 13 shows the relative motion amplitude in the frequency domain when only varying the impact stiffness (i.e., $k_1 = 50$ N/m, $k_2 = 200$ N/m, $k_3 = 500$ N/m, $k_4 = 1000$ N/m, and $k_5 = 5000$ N/m). A clear trend is that a larger impact stiffness gives rise to a noticeable resonant frequency shift and a drop in amplitude due to the impact-induced hardening effect. A large impact stiffness causes an irregular dynamic response in the impact region, such as WBTEH-3 mm-3 m/s²- k_5 and WBTEH-3 mm-6 m/s²- k_5 . Fig. 13(a.2) plots the displacement response of WBTEH-3 mm-3 m/s²- k_5 at 18.1 Hz in the time domain. It has sharp peaks with non-constant amplitude, indicating a rigid impact with a short engaging duration. The displacement response of WBTEH-3 mm-6 m/s²- k_5 at 18.1 Hz is plotted in Fig. 13(b.1). Once the excitation frequency exceeds 21 Hz, an interesting quasi-periodic motion, as shown in Fig. 13(b.2), occurs. The quasi-periodic response contains a frequency apart from the excitation

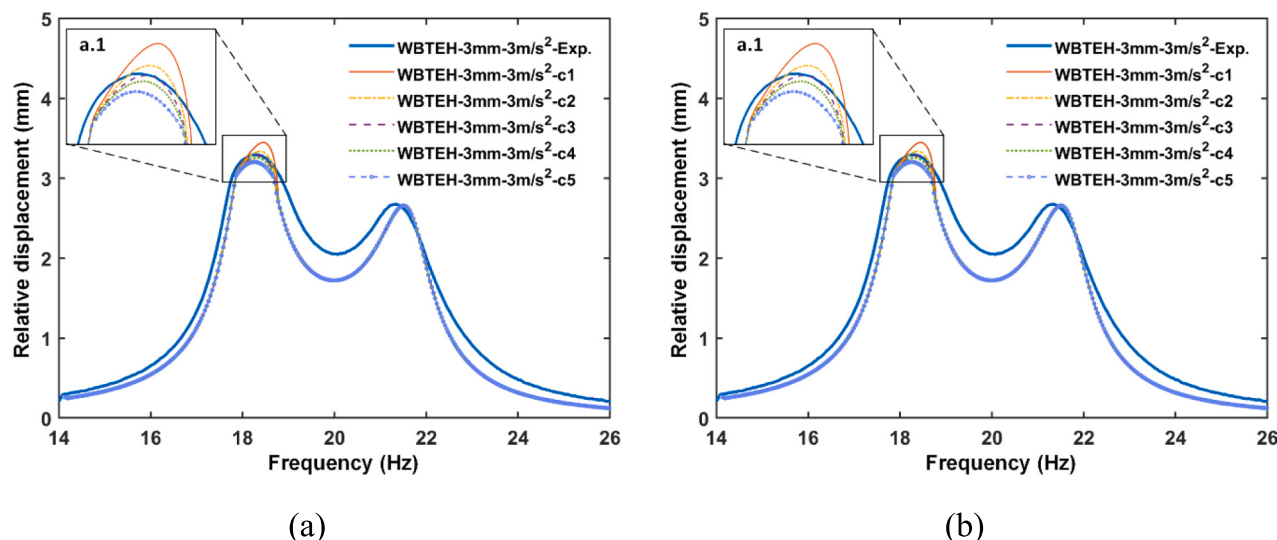


Fig. 14. Influence of impact damping on the dynamic response of the harvester.

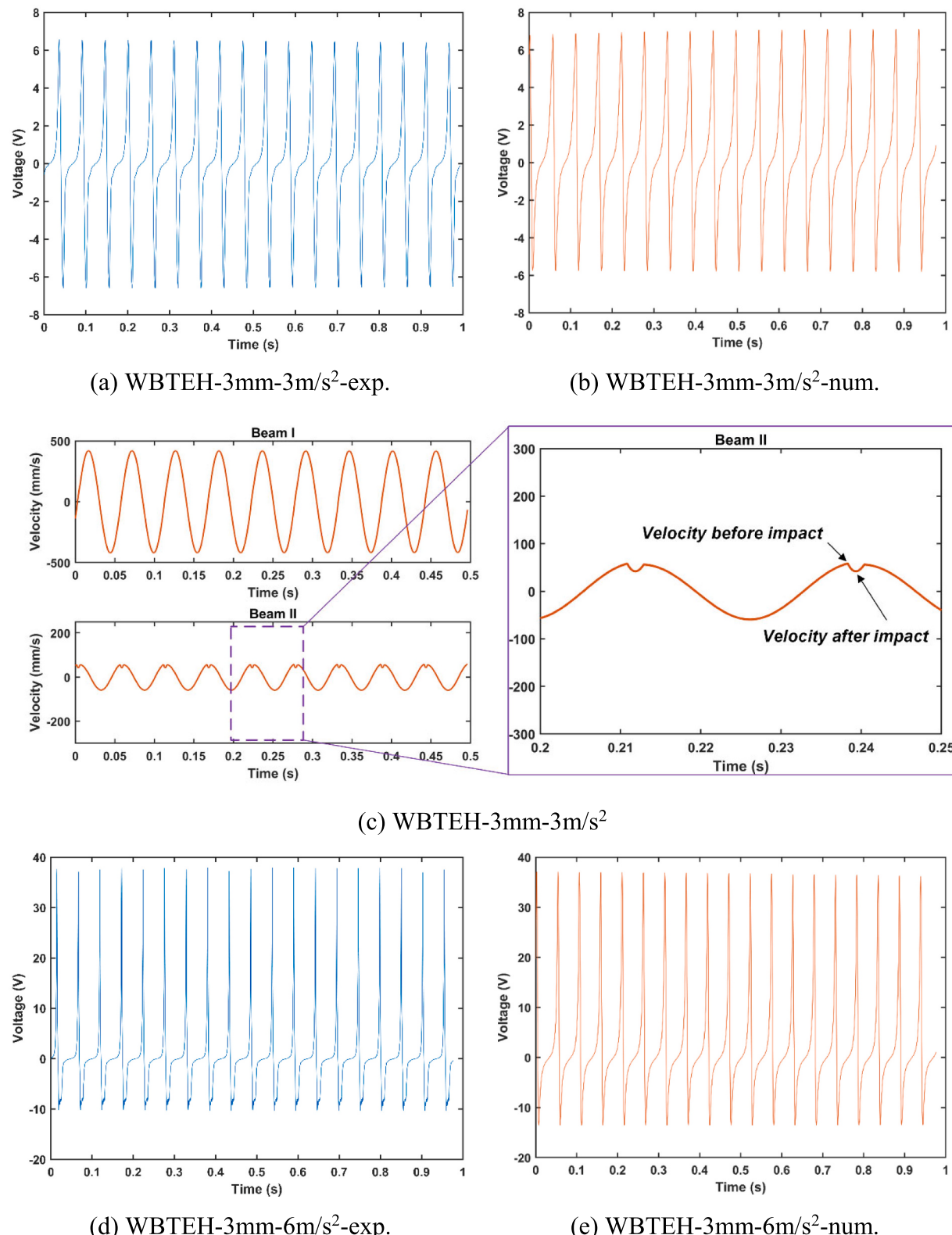


Fig. 15. Comparison of time-domain voltage signals and velocity waveforms obtained in the experiment and numerical simulation for WBTEH-3 mm under different accelerations.

frequency called beat frequency. The beat phenomenon happens when two oscillations with a similar frequency and varying phase superpose together, leading to a waxing and waning of the obtained displacement curve [35]. The beat frequency is approximately equal to the difference

between the two resonant frequencies ($\omega_{n2}-\omega_{n1}$). The simulated results of WBTEH-3 mm-3 m/s²-k2 and WBTEH-3 mm-6 m/s²-k4 agree with the corresponding experimental results, validating the correctness of the utilized impact stiffness. Here, $k2 = 200$ N/m, and $k4 = 1000$ N/m

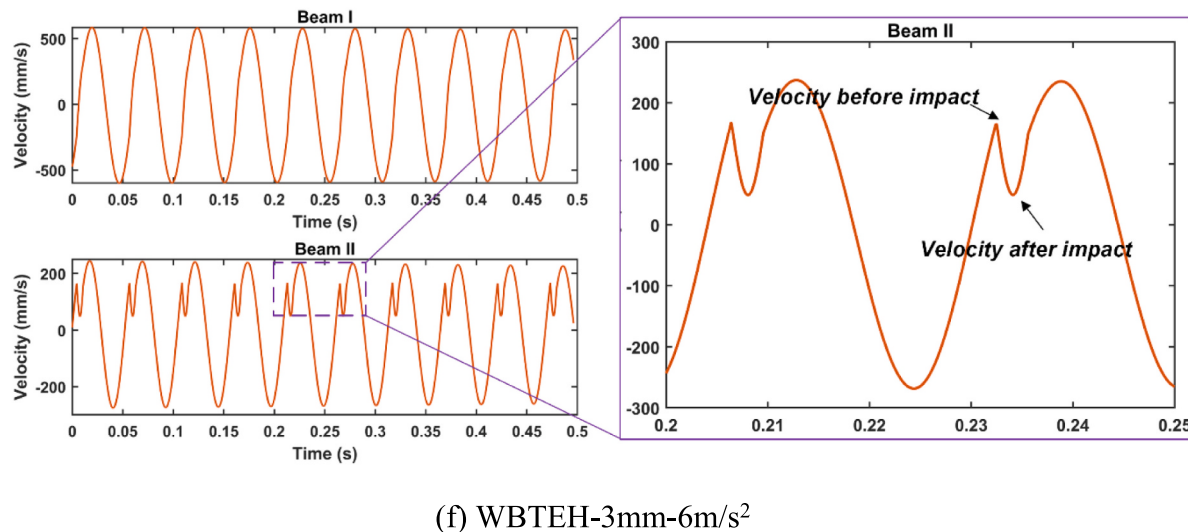


Fig. 15. (continued).

Table 4
Parameters used in the modeling.

Parameters	3 m/s ²	6 m/s ²
Contact stiffness, k_c	200 N/m	1000 N/m
Damping coefficient of stopper, c_c	1.5 N·s/m	2.0 N·s/m
Modal damping ratio, ζ_r	$\zeta_1 = 0.023, \zeta_2 = 0.026$	$\zeta_1 = 0.026, \zeta_2 = 0.050$
Surface charge density, σ	$1.53 \times 10^{-5} \text{ C/m}^2$	$2.86 \times 10^{-5} \text{ C/m}^2$

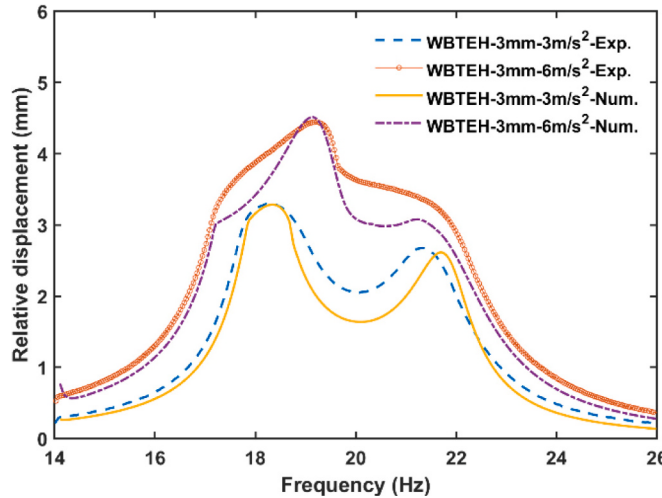
implies that the impact stiffness could vary with base excitations. In general, a large acceleration results in an extremely large impact stiffness. The analysis also shows that the rigid impact is unfavorable in practice due to the resultant nonpredictable dynamic response.

In addition to the impact stiffness, damping is another factor that affects the dynamics of the WBTEH. Fig. 14 shows the simulation results of WBTEH-3 mm under different base accelerations (3 m/s² and 6 m/s²) with different impact damping coefficients ($c_1 = 0.5 \text{ N}\cdot\text{s}/\text{m}$, $c_2 = 1.0 \text{ N}\cdot\text{s}/\text{m}$, $c_3 = 1.5 \text{ N}\cdot\text{s}/\text{m}$, $c_4 = 2 \text{ N}\cdot\text{s}/\text{m}$, and $c_5 = 5.0 \text{ N}\cdot\text{s}/\text{m}$). It is clear that the impact damping coefficient affects both the resonant frequency and

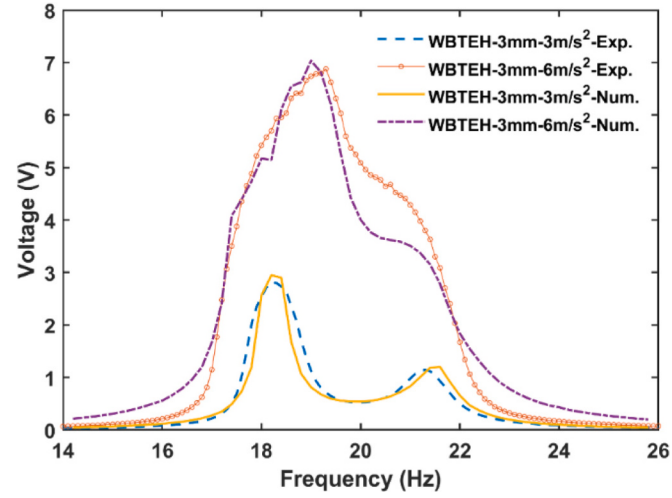
amplitude. $c_3 = 1.5 \text{ N}\cdot\text{s}/\text{m}$ represents the best prediction of the experimental results. Moreover, WBTEH-3 mm-3 m/s²- c_3 and WBTEH-3 mm-6 m/s²- c_4 have similar impact damping coefficients, indicating that the impact damping is less sensitive to the base excitation. Moreover, the impact damping is less influential than the impact stiffness. Furthermore, beat vibration occurs for WBTEH-3 mm-6 m/s²- c_1 with a small damping coefficient. According to all the simulations, the impact stiffness and damping coefficient are identified in the model validation.

6.2. Voltage output predictions

The coupled model is analyzed using the identified impact stiffness and damping coefficient via parameter identification. Fig. 15 compares the numerically simulated and experimentally measured voltage outputs. In cases where the impact between the beams is relatively soft and the excitation is small, symmetric voltage profiles are observed, as shown in Fig. 15(a) and (b). In this scenario, beam I oscillates at a relatively high velocity and interacts with beam II, as depicted in Fig. 15(c). We can observe a slight drop in vibrating velocity after the impact, resulting in minor energy loss. As a result, a symmetric voltage signal is



(a) Relative displacement



(b) RMS voltage

Fig. 16. Comparison between experimental and numerical results in the frequency domain for WBTEH-3 mm in terms of (a) Amplitude; (b) RMS voltage.

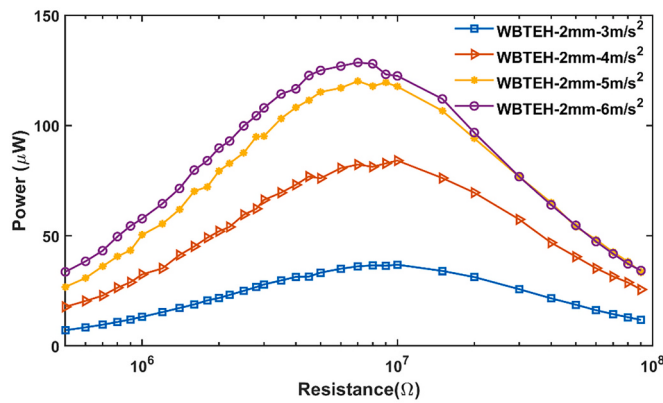


Fig. 17. Power variation of WBTEH with different external resistance under various base excitation.

obtained. However, when a significant impact occurs under a large excitation, the reduction in velocity for the two contact layers becomes substantial. This leads to a slower charge transfer process and generates an asymmetric peak-to-peak voltage signal, as illustrated in Fig. 15(d), (e), and (f). The extremely high positive voltage peak corresponds to the high velocity when the two layers approach each other, while the small negative peak is related to the velocity drop after the impact, indicating slow motion when the two layers separate. By comparing the velocities before and after the impact, it can be concluded that a significant impact causes significant energy dissipation, which in turn affects the performance of the WBTEH. Moreover, it can be seen that the simulated voltage signals are almost identical to the experimental ones. The theoretical model successfully predicted and captured not only the symmetric voltage feature at a low acceleration excitation but also the asymmetric voltage feature at a high acceleration excitation. When impact occurs, it is necessary to incorporate the impact force into the model. However, quantifying the impact stiffness and damping parameters proves challenging. Therefore, these two parameters are determined through trial and error within a reasonable range. Different combinations of impact stiffness and damping parameters are tested in simulations until the correct set is found, producing numerical results

that align with experimental results. The determined model parameters are listed in Table 4. The net surface charge accumulated on the material will saturate after a few contact-separation cycles and maintain constant afterward. However, effectively transferred charges may vary under different contact conditions. It is found that the effective charge density increases with accelerations for the proposed WBTEH, which has been proven by the charge measurement results using an electrometer. Besides, at the base acceleration of 6 m/s², the damping ratios of the beams are tuned to match the experimental results based on the measured damping ratios, which are difficult to identify using the logarithmic attenuation method when a huge impact is engaged at a large acceleration.

The voltage output of the WBTEH in the frequency domain is thoroughly investigated. Fig. 16(a) shows the amplitude of the relative motion ($w = w_2 - w_1$) between the two beams, and Fig. 16(b) shows the corresponding RMS voltage. It can be seen that the displacement curve shares a similar pattern with the voltage curve, which is because the harvester's performance is closely related to the relative motion of the triboelectric layers. The simulated results show good agreement with the experimental ones in terms of both displacement and voltage, although discrepancies appear after the locking frequency. This might be due to the complexity of the impact-related damping behavior at a large acceleration. After all, the above results have shown that the developed theoretical model can capture the overall trend and peaks of the WBTEH.

7. Performance characterization of WBTEH

This section aims to investigate the optimal power output of the WBTEH. WBTEH-2 mm is selected as an example, and the impedance matching test is conducted. The rectified voltage is connected to an adjustable resistor, and the voltage applied to the resistor is recorded. The power can be calculated using the formula $P = V^2/R$. Fig. 17 shows that the maximum power can reach 129 μW for WBTEH-2 mm-6 m/s², and the corresponding resistance is 7 M Ω . Even at the acceleration of 3 m/s², the harvester can produce an optimal output of 37 μW . However, the matched resistance is increased to 10 M Ω . A general trend is that the optimal resistance decreases with increased base excitation, which is reasonable since the higher the acceleration, the better the contact



Fig. 18. Demonstration of using a prototyped WBTEH to power a sensor node and transmit signal wirelessly: (a) experimental setup; (b) mobile app displaying the temperature and location data; (c) laptop dashboard showing temperature with alarm function.

between the triboelectric layer is, leading to the decrement of the internal impedance of the WBTEH. Thus, WBTEH-2 mm-6 m/s² has a smaller matched resistance.

One ultimate goal of developing energy harvesters is to power sensor nodes by using the harnessed energy from the ambient environment. In order to evaluate the performance of the harvester, WBTEH-2 mm-6 m/s²-A is used for demonstration in the lab, considering its best power output at locking frequency. Fig. 18(a) shows the overall setup. In brief, the shaker provides the harmonic base excitation that simulates the ambient vibration source. The harvester is mounted on the shaker, and the output of the harvester is connected to an energy management unit (EMU) with an embedded temperature sensor to monitor the surrounding temperature. The harvested electricity is stored in a capacitor with a capacitance of 47 μF. A multimeter monitors the charging voltage of the capacitor. It can be observed that the capacitor can be charged to 5 V in 100 s. Once it reaches 5 V, the sensor starts working and consuming the electricity from the capacitor. After that, the capacitor voltage drops quickly to around 3.5 V and gradually re-rises to 5 V if the harvester works continuously. According to the eq. $P = 0.5 \cdot C U^2 / \Delta t$, the average power of WBTEH-2 mm-6 m/s² is estimated to be 5.9 μW. However, this power value is much smaller than the optimal power output. This discrepancy can be attributed to impedance mismatch and capacitor discharge, which affect the overall energy transfer and conversion efficiency of the harvester. In Fig. 18(b), the mobile screen displays the room temperature of 25.5 degrees and the sensor's location on the map. In wireless sensing, the sensor nodes usually send data to the cloud via the gateway to conquer the distance limitation. The user can view the data using mobile terminals anywhere at any time as long as the internet is accessible. To check whether the sensor can measure the temperature change, a hot-blowing gun is used to change the environment temperature around the sensor. We intentionally set an alarm temperature as 50 degrees. Fig. 18(c) shows that the data can be sent to the cloud and displayed on a web-based dashboard, and the background color turns from green to red once the measured temperature exceeds the configured alarming threshold.

8. Conclusion

In this study, a WBTEH with a dual-beam structure has been proposed and evaluated for broadband energy harvesting. The electromechanical model of the WBTEH was formulated and validated. WBTEH prototypes were fabricated and tested. The key findings are summarized as follows.

- The gap distance between the triboelectric layers affects the bandwidth and power output of the WBTEH. For example, WBTEH-5 mm can only achieve a discrete bandwidth in the acceleration range from 3 m/s² to 6 m/s². In contrast, WBTEH-2 mm exhibits a continuous bandwidth, and its power is much larger than that of WBTEH-5 mm in the same frequency range. Meanwhile, a too small gap distance is not recommended, such as WBTEH-0 mm with a quasi-zero gap distance having a very limited bandwidth. Among all the tested prototypes, a 2 mm gap was found to be optimal for the proposed WBTEH.
- The WBTEH exhibits frequency locking behavior when the displacement amplitude/gap ratio exceeds 1.48. Strong nonlinear resonance with a large vibration amplitude occurs when the WBTEH is excited at the locking frequency, leading to a continuous bandwidth with a significantly large power output. Unlike purely impact-based TEHs, the WBTEH demonstrated excellent stability with matched voltage peaks and bandwidth in the frequency up-sweep and down-sweep tests.
- The formulated electromechanical model captured the key features of the WBTEH, such as the symmetric and asymmetric voltage profiles in the time domain and the voltage frequency response in the frequency domain. The parametric study has revealed that the

impact stiffness and damping greatly influence the performance of WBTEH. Generally, a large impact stiffness and a small damping induce the beating phenomenon, resulting in non-constant voltage outputs.

- The WBTEH prototype successfully powered a temperature sensor node that wirelessly transmitted the signal to the mobile/computer via a gateway, demonstrating the excellent potential of the WBTEH for IoT applications.
- The broadband capability of the proposed WBTEH is achieved based on the combination of impact nonlinearity and multi-resonance method. This study only involves two resonant frequencies from two cantilever beams. Future development of the harvester with more resonant frequencies and modes could result in an ultra-bandwidth TEH in the low-frequency range.

Overall, the WBTEH design offers a promising energy harvesting solution using triboelectric materials, particularly for applications where wide bandwidth and stability are crucial. The study provides a detailed analysis of the harvester's performance and the effects of design parameters. Some key findings from this work and the mechanisms discussed in this paper can guide the development of more efficient and reliable energy harvesters in the future.

CRediT authorship contribution statement

Chaoyang Zhao: Writing – original draft, Methodology, Conceptualization. **Guobiao Hu:** Writing – review & editing, Investigation. **Xin Li:** Software, Methodology. **Zicheng Liu:** Methodology, Data curation. **Weifeng Yuan:** Supervision. **Yaowen Yang:** Writing – review & editing, Supervision.

Declaration of Competing Interest

The authors declare that they have no known competing financial interests or personal relationships that could have appeared to influence the work reported in this paper.

Data availability

Data will be made available on request.

References

- Dong L, Closso AB, Jin C, Tras I, Chen Z, Zhang JX. Vibration-energy-harvesting system: transduction mechanisms, frequency tuning techniques, and biomechanical applications. *Adv Mater Technol* 2019;4:28.
- Kim H, Tai WC, Parker J, Zuo L. Self-tuning stochastic resonance energy harvesting for rotating systems under modulated noise and its application to smart tires. *Mechan Syst Sign Proc* 2019;122:769–85.
- Upadrashta D, Yang Y. Trident-shaped multimodal piezoelectric energy harvester. *J Aerospace Eng* 2018;31.
- Li X, Yu K, Upadrashta D, Yang Y. Comparative study of core materials and multi-degree-of-freedom sandwich piezoelectric energy harvester with inner cantilevered beams. *J Phys D Appl Phys* 2019;52.
- Jung SM, Yun KS. Energy-harvesting device with mechanical frequency-up conversion mechanism for increased power efficiency and wideband operation. *Appl Phys Lett* 2010;96.
- Halim MA, Park JY. Theoretical modeling and analysis of mechanical impact driven and frequency up-converted piezoelectric energy harvester for low-frequency and wide-bandwidth operation. *Sens Actuator A-Phys* 2014;208:56–65.
- Li Z, Saadatnia Z, Yang Z, Naguib H. A hybrid piezoelectric-triboelectric generator for low-frequency and broad-bandwidth energy harvesting. *Energ Convers Manage* 2018;174:188–97.
- Hu G, Zhao C, Yang Y, Li X, Liang J. Triboelectric energy harvesting using an origami-inspired structure. *Appl Energy* 2022;306.
- Rasel MSU, Park J-Y. A sandpaper assisted micro-structured polydimethylsiloxane fabrication for human skin based triboelectric energy harvesting application. *Appl Energy* 2017;206:150–8.
- Cheng J, Ding W, Zi Y, Lu Y, Ji L, Liu F, et al. Triboelectric microplasma powered by mechanical stimuli. *Nat Commun* 2018;9:3733.
- Yu YH, Wang XD. Chemical modification of polymer surfaces for advanced triboelectric nanogenerator development. *Extreme Mech Lett* 2016;9:514–30.

- [12] Bae J, Lee J, Kim S, Ha J, Lee BS, Park Y, et al. Flutter-driven triboelectrification for harvesting wind energy. *Nat Commun* 2014;5:4929.
- [13] Su L, Wang H, Tian Z, Wang H, Cheng Q, Yu W. Low detection limit and high sensitivity wind speed sensor based on Triboelectrification-induced electroluminescence. *Adv Sci (Weinh)* 2019;6:1901980.
- [14] Wang JL, Geng LF, Ding L, Zhu HJ, Yurchenko D. The state-of-the-art review on energy harvesting from flow-induced vibrations. *Appl Energy* 2020;267.
- [15] Liang X, Jiang T, Liu G, Xiao T, Xu L, Li W, et al. Triboelectric Nanogenerator networks integrated with power management module for water wave energy harvesting. *Adv Funct Mater* 2019;29.
- [16] Lin ZH, Cheng G, Lee S, Pradel KC, Wang ZL. Harvesting water drop energy by a sequential contact-electrification and electrostatic-induction process. *Adv Mater* 2014;26:4690–6.
- [17] Yang S, Su Y, Xu Y, Wu Q, Zhang Y, Raschke MB, et al. Mechanism of electric power generation from ionic droplet motion on polymer supported graphene. *J Am Chem Soc* 2018;140:13746–52.
- [18] Dhakar L, Tay FEH, Lee CK. Investigation of contact electrification based broadband energy harvesting mechanism using elastic PDMS microstructures. *J Micromech Microeng* 2014;24.
- [19] Ibrahim A, Ramini A, Towfighian S. Triboelectric energy harvester with large bandwidth under harmonic and random excitations. *Energy Rep* 2020;6:2490–502.
- [20] Qi Y, Kuang Y, Liu Y, Liu G, Zeng J, Zhao J, et al. Kirigami-inspired triboelectric nanogenerator as ultra-wide-band vibrational energy harvester and self-powered acceleration sensor. *Appl Energy* 2022;327:120092.
- [21] Gupta RK, Shi QF, Dhakar L, Wang T, Heng CH, Lee C. Broadband energy harvester using non-linear polymer spring and electromagnetic/triboelectric hybrid mechanism. *Sci Rep* 2017;7.
- [22] Fu Y, Ouyang H, Benjamin Davis R. Nonlinear structural dynamics of a new sliding-mode triboelectric energy harvester with multistability. *Nonlinear Dynam* 2020;100:1941–62.
- [23] Tan D, Zhou J, Wang K, Zhao X, Wang Q, Xu D. Bow-type bistable triboelectric nanogenerator for harvesting energy from low-frequency vibration. *Nano Energy* 2022;92:106746.
- [24] Luo H, Liu J, Yang T, Zhang Y, Cao Q. Dipteron flight-inspired bistable triboelectric nanogenerator for harvesting low frequency vibration. *Nano Energy* 2022;103:107755.
- [25] Li X, Upadrashta D, Yu K, Yang Y. Analytical modeling and validation of multi-mode piezoelectric energy harvester. *Mechan Syst Sign Proc* 2019;124:613–31.
- [26] Tao K, Tang L, Wu J, Lye SW, Chang H, Miao J. Investigation of multimodal electret-based MEMS energy harvester with impact-induced nonlinearity. *J Microelectromech Syst* 2018;27:276–88.
- [27] Zhao CY, Yang YW, Upadrashta D, Zhao LY. Design, modeling and experimental validation of a low-frequency cantilever triboelectric energy harvester. *Energy* 2021;214.
- [28] Erturk A, Inman DJ. On mechanical modeling of cantilevered piezoelectric vibration energy harvesters. *J Intellig Mater Syst Struct* 2008;19:1311–25.
- [29] Erturk Ai DJ. Mechanical considerations for modeling of vibration-based energy harvesters. In: Proceedings of the ASME IDETC 21st Biennial Conference on Mechanical Vibration and Noise; 2007. 4–7 September 2007.
- [30] Reboças GfdS, Santos IF, Thomsen JJ. Validation of vibro-impact force models by numerical simulation, perturbation methods and experiments. *J Sound Vib* 2018;413:291–307.
- [31] Gandhi PS, Vyas V. On the dynamics of tapered vibro-impacting cantilever with tip mass. *J Mechani Sci Technol* 2017;31:63–73.
- [32] Fu Y, Ouyang H, Davis RB. Effects of electrical properties on vibrations via electromechanical coupling in triboelectric energy harvesting. *J Phys D Appl Phys* 2020;53:215501.
- [33] Zhang W, Li X, Ye Z, Jiang Y. Mechanism of frequency lock-in in vortex-induced vibrations at low Reynolds numbers. *J Fluid Mech* 2015;783:72–102.
- [34] Sim W, Lee B, Kim DJ, Lee JA, Kim J, Chung J. Vibro-impact analysis of two adjacent cantilever beams. *Nonlinear Dynam* 2022;108:987–1004.
- [35] Rittweger J. Manual of vibration exercise and vibration therapy. Springer; 2020.